

Image-enhanced thermal-wave slice diffraction tomography with numerically simulated reconstructions

Lena Nicolaides and Andreas Mandelis

Photothermal and Optoelectronic Diagnostics Laboratories, Department of Mechanical Engineering, University of Toronto, and Manufacturing Research Corporation of Ontario (MRCO), 5 King's College Road, Toronto, Ontario, Canada M5S 3G8

Received 5 August 1996, in final form 18 July 1997

Abstract. Thermal-wave slice diffraction tomography (TSDT) is a photothermal imaging technique for non-destructive evaluation (NDE), leading to the detection of subsurface cross sectional defects in opaque solids in the very-near-surface region (μm – mm). An exact, Green's-function based mathematical model that represents the behaviour of a three-dimensional thermal wave is developed and correlated with a numerical reconstruction technique. The computational technique utilizes the well known Tikhonov regularization method to invert almost singular matrices resulting from the ill-posedness of the inverse thermal-wave problem for the reconstruction of thermal diffusivity cross sectional images in materials. Numerical calculations of the inverse problem are carried out using the Born approximation and simulated reconstructions in back scattering and transmission are presented.

1. Introduction

Thermal-wave slice diffraction tomography (TSDT) is a photothermal imaging technique for non-destructive evaluation (NDE), leading to the detection of subsurface cross sectional defects in opaque solids in the very-near-surface region (μm – mm). Thermal-wave tomography refers to cross sectional imaging of the thermal diffusivity of an object upon reconstruction from its projections from different directions. This calls for an inversion technique which can reconstruct the defect from experimental thermal-wave cross sectional data.

Images obtained from conventional thermal-wave imaging are two-dimensional 'projections' of subsurface features. These images are projections in the sense that the image is formed by mapping the sample surface temperature in a two-dimensional raster without regard to the actual depth position of scatterers. Although work has been done in obtaining depth information on subsurface features [1, 2] and depth profiling of layered samples, using equivalent experimental techniques, no work has been reported until recently in obtaining tomographic images using thermal waves. A photothermal method based on the mirage effect was utilized to obtain depth information on the presence of defects by means of a tomographic-like procedure [3] but due to the line-integral nature of the probe beam, this technique cannot yield proper tomographic inversions.

The first rigorous implementation of TSDT, which detected scan data by photopyroelectric detection [4], followed a reconstruction algorithm based on the ray-like propagation of thermal waves [5, 6]. The limitations of this method suggested a consideration of a diffractive propagation approach for thermal waves. A high-fidelity

tomographic imaging, ray-based, reconstruction method for photopyroelectric thermal detection was later demonstrated by Yarai *et al* [7]. To overcome the limitations of a ray-optic tomographic reconstruction and to account for the highly dispersive and spatially damped nature of pseudopropagating thermal waves, a method was further developed by Padé and Mandelis [8,9]. The imaged quantity was the cross sectional thermal diffusivity. The method was successful in developing a mathematical process to deal with the ill-conditioning of thermal waves, by the Tikhonov regularization method, but it addressed the physical behaviour of thermal waves only approximately. The technique approximated the wave field with a two-dimensional Green's function on the slice cross section. This resulted in adequate reconstructions, in specific cases, in cross sections away from the incident laser-source range, where a strong singularity was pronounced. This behaviour is typical of two-dimensional propagating wavefields, and is shared by the pseudopropagating thermal-wave problem. In order to avoid the strong two-dimensional singularity at the origin, a three-dimensional formulation of the problem is needed, with Green's function to be described over a cross sectional area normal to the surface and at fixed lateral coordinate.

Unlike electromagnetic or acoustic tomography, thermal-wave tomography suffers from the following relative setbacks: (a) propagation distances of the thermal wave are short, (b) the thermal wavevector is complex, lying along the 45° line in the complex plane [10], (c) the sample cannot be rotated in most practical situations [5]. Therefore, the conventional reconstruction used in well-posed propagating wavefield tomographies [11] cannot be applied in the case of the thermal-wave problem. A rigorous mathematical model that represents the behaviour of three-dimensional thermal waves, rather than the earlier approximate models [5–9], is developed and correlated with a numerical reconstruction technique. This paper is focused on the new application of a recently developed theoretical expression of Green's function for the three-dimensional Helmholtz pseudowave equation [12] to the solution of the incident harmonic temperature field; and its computational implementation and correlation with the well known Tikhonov regularization method to solve the discrete thermal-wave ill-posed problem. The work is in two parts: (a) a theoretical model that describes the behaviour of thermal waves in three-dimensional space (*forward process*), (b) a numerical technique that will produce a tomogram from simulated data (*inverse process*).

2. Forward process: thermal-wave diffraction theory

The physical geometry of the problem is shown in figure 1 where two possible embodiments of the thermal-wave slice tomographic configuration include a focused laser-beam source scanned along the spatial coordinate $(x, 0)$ and a thermal-wave detector on the laser side (back-scattered tomography) or on the opposite side (transmission tomography) of the sample. The laser fluence is modulated at a constant frequency $f = \omega/2\pi$ where ω is the angular modulation frequency. Upon absorption on the opaque sample surface and optical-to-thermal energy conversion, the modulated optical radiation generates a surface-localized harmonically oscillating temperature ('thermal-wave') field. The latter, driven by thermal gradients into the bulk of the solid, may encounter thermal discontinuities (defects, cracks, inclusions) and scatter. The detector(s) pick up amplitude and phase signals which contain information about the scattering process. The inverse problem consists in deconvoluting this information from that associated with the forward propagating thermal-wave field, and reconstructing the slice thermal diffusivity image from data generated by scanning the laser-source coordinate and with stationary detector(s), or vice versa [13]. The mathematical theory of the thermal-wave propagation process is developed utilizing

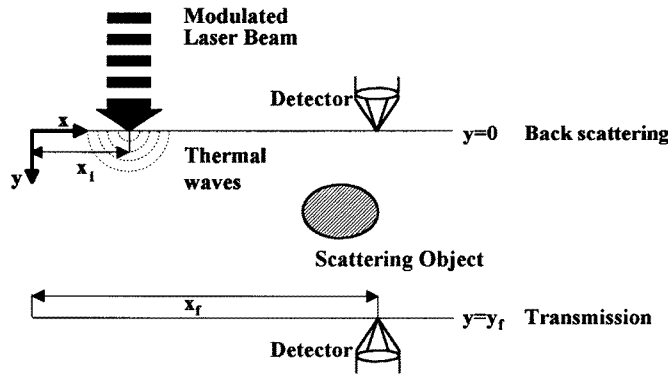


Figure 1. The geometry for TSDT amenable to back-scattering and transmission detection.

thermal-wave diffraction [10] (the forward process).

In the case of a harmonic photothermal excitation of a region in space, the temperature is found to obey the Helmholtz pseudowave equation [10, 14]

$$(\nabla^2 + q^2(\mathbf{r}))T(\mathbf{r}) = 0 \quad (1)$$

where

$$q(\mathbf{r}) = (1 + i) \left[\frac{\omega}{2\alpha(\mathbf{r})} \right]^{1/2} \quad (2)$$

is the complex thermal wavenumber; $\alpha(\mathbf{r})$ is the thermal diffusivity of the medium in which the thermal wave is excited and pseudopropagates. Letting the thermal diffusivity of the assumed homogeneous medium surrounding the object region Q be α_0 , equation (1) may be replaced by a modified Helmholtz pseudowave equation [10]

$$(\nabla^2 + q_0^2)T(\mathbf{r}) = -F(\mathbf{r})T(\mathbf{r}) \quad (3)$$

where

$$F(\mathbf{r}) = \begin{cases} q_0^2[n^2(\mathbf{r}) - 1] & \mathbf{r} \in Q \\ 0 & \mathbf{r} \notin Q. \end{cases} \quad (4)$$

Furthermore, $q_0(\omega)$ is the thermal wavenumber,

$$q_0(\omega) = (1 + i) \left(\frac{\omega}{2\alpha_0} \right)^{1/2} = |q_0(\omega)|e^{i\pi/4} \quad (5)$$

$$n(\mathbf{r}) \equiv \left[\frac{\alpha_0}{\alpha(\mathbf{r})} \right]^{1/2}. \quad (6)$$

$n(\mathbf{r})$ is a measure of the variation of the values of the thermal diffusivity in the scattering object Q from that of the surrounding (reference) region Q_0 . The ratio in equation (6) has been symbolized by $n(\mathbf{r})$ deliberately, to suggest the analogy of this parameter to the effects of variations in the refractive index in conventional optical propagating fields. The effect of the inhomogeneities of object region Q appear as a source function in the right side of equation (3), with $F(\mathbf{r})$ being the object function, representing the inhomogeneities of scattering-object region Q . The object function $F(\mathbf{r})$ is zero at every point outside region Q and has a non-zero value that represents the ratio of thermal diffusivities inside region Q .

The exact solution for the scattering field of equation (3) satisfies, in three dimensions [15, 16],

$$T_s(\mathbf{r}) = \iiint_R G_0(\mathbf{r}|\mathbf{r}_0)F(\mathbf{r}_0)T(\mathbf{r}_0) d^3\mathbf{r}_0 \quad (7)$$

which is the Fredholm integral equation of the second kind needed for solving the inverse problem. $T(\mathbf{r})$ is the total thermal-wave field. Region R is a cross sectional slice in two-dimensional space, and is of constant thickness. An approximate solution can be written using the Born approximation, valid for the case when the object is weakly inhomogeneous, and the scattering field is weak and much smaller than the total field, $|T_s(\mathbf{r})| \ll |T(\mathbf{r})|$ [11],

$$T_s(\mathbf{r}) \simeq T_{\text{born}}(\mathbf{r}) = \iiint_R G_0(\mathbf{r} - \mathbf{r}_0)F(\mathbf{r}_0)T_i(\mathbf{r}_0) d^3\mathbf{r}_0 \quad (8)$$

where $T_i(\mathbf{r})$ is the incident homogeneous thermal-wave field, representations of which are derived in section 2.1 for semi-infinite and bounded three-dimensional geometries. The accuracy of the first Born approximation increases when the scattered field becomes much smaller than the incident field.

2.1. Homogeneous thermal-wave field

For a surface source only, the solution to the homogeneous thermal-wave equation is,

$$T_i(\mathbf{r}, \omega) = \alpha \iint_{S_0} [G_0(\mathbf{r} - \mathbf{r}_0^s, \omega)\nabla_0 T(\mathbf{r}_0^s, \omega) - T(\mathbf{r}_0^s, \omega)\nabla_0 G_0(\mathbf{r} - \mathbf{r}_0^s, \omega)] \cdot d\mathbf{S}_0 \quad (9)$$

where S_0 is the surface surrounding the source volume V_0 . $d\mathbf{S}_0$ must be replaced by $d\mathbf{S}_i = \hat{\mathbf{n}}_i dx_0 dy_0$ pointing in the direction inside the material volume, V_0 , to indicate the in-flow of thermal energy; \mathbf{r}_0^s is a coordinate point on S_0 . $T(\mathbf{r}_0^s, \omega)$ is the thermal-wave field distribution on the optically heated material surface. The thermal diffusivity, α , and the thermal conductivity, k , are assumed to be constant throughout V_0 .

Thermal-wave flux, ϕ , is prescribed over the interface plane, $z_0 = 0$,

$$\phi(\mathbf{r}_s, t) = \phi_0 e^{-r_s^2/w^2} e^{i\omega t} \quad (10)$$

generated by a Gaussian laser beam of spot-size w . If the thermal-wave flux is prescribed at the interface, $z = 0$, the Green's function must satisfy homogeneous Neumann boundary conditions at the source coordinate, $z_0 = 0$. For the finite geometry of figure 1, the method of images can be used to accommodate plane bounding surfaces at $z = 0, L$. The resulting Green's function is [12],

$$G_0(\mathbf{r} - \mathbf{r}_0|\mathbf{r} - \mathbf{r}'_0, \omega) = \frac{1}{4\pi\alpha} \sum_{n=-\infty}^{\infty} \left(\frac{e^{-q_0(\omega)|\mathbf{r}-\mathbf{r}_{0n}|}}{|\mathbf{r} - \mathbf{r}_{0n}|} + \frac{e^{-q_0(\omega)|\mathbf{r}-\mathbf{r}'_{0n}|}}{|\mathbf{r} - \mathbf{r}'_{0n}|} \right) \quad (11)$$

where, figure 2,

$$|\mathbf{r} - \mathbf{r}_{0n}| = \sqrt{(x - x_0)^2 + (y - y_0)^2 + [z - (2nL + z_0)]^2} \quad (12a)$$

and

$$|\mathbf{r} - \mathbf{r}'_{0n}| = \sqrt{(x - x_0)^2 + (y - y_0)^2 + [z - (2nL + z_0)]^2} \quad (12b)$$

and $q_0(\omega)$ is the complex thermal wavenumber.

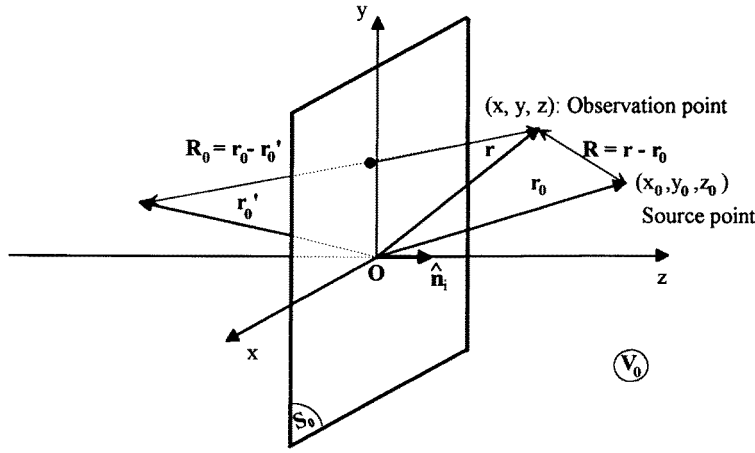


Figure 2. The coordinate system for three-dimensional geometry.

2.1.1. *Semi-infinite solid.* Green’s function for the semi-infinite solid geometry is given by [12]

$$G_0(\mathbf{r} - \mathbf{r}_0 | \mathbf{r} - \mathbf{r}'_0, \omega) = \frac{1}{4\pi\alpha} \left(\frac{e^{-q_0(\omega)|\mathbf{r}-\mathbf{r}_0|}}{|\mathbf{r} - \mathbf{r}_0|} + \frac{e^{-q_0(\omega)|\mathbf{r}-\mathbf{r}'_0|}}{|\mathbf{r} - \mathbf{r}'_0|} \right). \quad (13)$$

For the homogeneous case, no volume sources exist in the half-space $z > 0$, as in figure 2. Therefore, from equation (9) the thermal-wave field becomes,

$$T_i(\mathbf{r}, \omega) = \alpha \iint_{S_0} G_0(\mathbf{r} - \mathbf{r}_0^s | \mathbf{r} - \mathbf{r}'_0^s, \omega) \nabla_0 T(\mathbf{r}_0^s, \omega) \cdot d\mathbf{S}_0. \quad (14)$$

The surface, S_0 , is the plane $z_0 = 0$. Combining equations (10), (13) and (14), the thermal-wave field in the form of an integral over the bounding interface, $S_0(x_0, y_0)$ [12], is

$$T_i(\mathbf{r}, \omega) = \frac{\phi_0}{2\pi k} e^{i\omega_0 t} \exp\left(-\frac{(x^2 + y^2)}{w^2}\right) J_3(x, y, z) \quad (15)$$

with

$$J_3(x, y, z) = 2\pi \int_0^\infty \frac{\rho}{\sqrt{\rho^2 + z^2}} \exp\left(-\frac{\rho^2}{w^2} - q_0(\omega)\sqrt{\rho^2 + z^2}\right) \mathbf{l}_0\left(\frac{2\rho}{w^2}\sqrt{x^2 + y^2}\right) d\rho. \quad (16)$$

\mathbf{l}_0 is the modified Bessel function of order zero. The thermal-wave field represented by equations (15) and (16) can be evaluated numerically using the polynomial approximation for $\mathbf{l}_0(x)$ given in [17, entries 9.8.1–9.8.4]. Integral J_3 has a removable singularity at $z = 0$, which makes it very attractive for programming. At $z = 0$, J_3 becomes,

$$J_3(x, y, 0) = 2\pi \int_0^\infty \exp\left(-\frac{\rho^2}{w^2} - q_0(\omega)\rho\right) \mathbf{l}_0\left(\frac{2\rho}{w^2}\sqrt{x^2 + y^2}\right) d\rho. \quad (17)$$

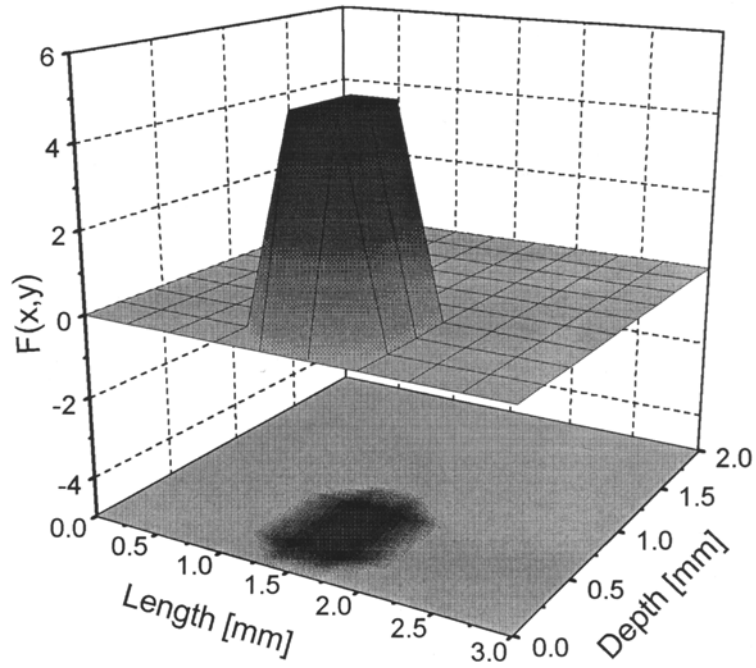


Figure 3. The forward process; three-dimensional relief of a simulated cross section with a hole centred at $(x_c, y_c) = (1.5 \text{ mm}, 0.5 \text{ mm})$; radius $a = 0.4 \text{ mm}$.

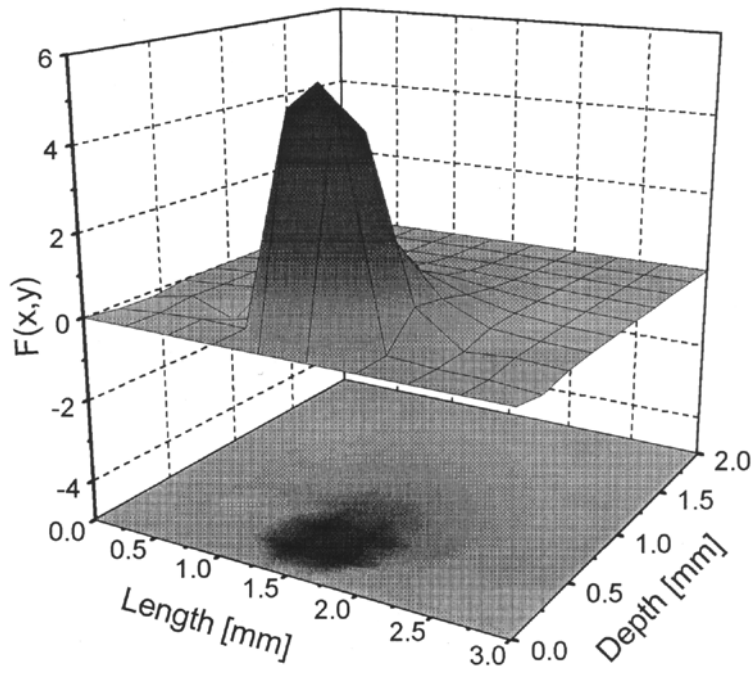


Figure 4. The inverse process—TSDT back-scattering reconstruction of the object function $F(x, y)$ of figure 3. Laser position at $x_l = 1 \text{ mm}$, $f = 15 \text{ Hz}$; regularization parameter $\sigma = 10^{-6}$.

2.1.2. Solid of finite thickness bounded between two planes. In the finite region, $z_0 = 0, L$, the thermal-wave flux is prescribed over the interface plane, $z_0 = 0$, generated by a Gaussian laser beam of spot-size w , given by equation (10). The thermal-wave field, equation (14), is simplified, with the thermal-wave flux being set to zero at $z_0 = L$. This is due to the large thermal mismatch between the matter enclosed between the bounding planes at 0 and L , and the surrounding medium, assumed to be a poor thermal conductor (air). The relevant Green's function is now equation (11), satisfying homogeneous Neumann conditions at both interface planes. Defining the integrals

$$J_4(x, y, A_n) = 2\pi \int_0^\infty \frac{\rho}{\sqrt{\rho^2 + A_n^2}} \exp\left(-\frac{\rho^2}{w^2} - q_0(\omega)\sqrt{\rho^2 + A_n^2}\right) \mathbf{I}_0\left(\frac{2\rho}{w^2}\sqrt{x^2 + y^2}\right) d\rho \quad (18)$$

results in the expression for the thermal-wave field

$$T_i(\mathbf{r}, \omega) = \frac{\phi_0}{2\pi k} e^{i\omega t} e^{-\frac{x^2 + y^2}{w^2}} \left\{ J_3(x, y, z) + \sum_{n=1}^\infty [J_4(x, y, 2nL - z) + J_4(x, y, 2nL + z)] \right\}. \quad (19)$$

The thermal-wave field at the sample surface $z = 0$ now becomes

$$T_i(x, y, 0; \omega_0) = \frac{\phi_0}{2\pi k} \exp\left(-\frac{x^2 + y^2}{w^2}\right) \left\{ J_3(x, y, 0) + \sum_{n=1}^\infty [J_4(x, y, 0) + J_4(x, y, 2nL)] \right\} \quad (20a)$$

and the thermal-wave field at the back surface $z = L$ becomes

$$T_i(x, y, L; \omega_0) = \frac{\phi_0}{2\pi k} \exp\left(-\frac{x^2 + y^2}{w^2}\right) \left\{ J_3(x, y, L) + 2 \sum_{n=1}^\infty J_4(x, y, 2nL) \right\}. \quad (20b)$$

These expressions are novel and exact representations of the homogeneous thermal-wave field in the solid. They can be used to reconstruct the inverse problem.

3. Inverse process: computational aspects

The foregoing thermal-wave diffraction problem leads to a so-called discrete ill-posed problem when solved numerically. In an ill-posed problem, small perturbations in the data of the problem cause large perturbations in the solution [18]. These problems are intrinsically difficult to solve, and, indeed, the standard methods in numerical linear algebra, such as LU - or QR -factorizations [19] cannot be used. Instead, a regularization method can be applied to stabilize the problem. In this work, the Tikhonov regularization method is used.

3.1. Formulation of equations

Region R in equation (7) is a slice in two-dimensional space, and it is assumed to be rectangular, with the photothermal excitation on one side of the region ($y = 0$), as in figure 1. The rectangular region is then

$$R = \{(x, y) | x_i \leq x \leq x_f, 0 \leq y \leq y_f\}. \quad (21)$$

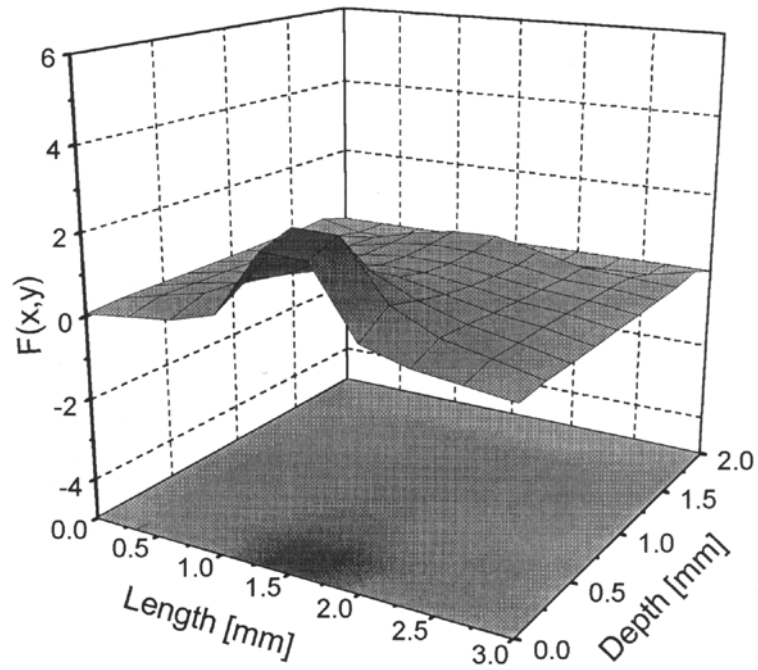


Figure 5. The inverse process-TSDT transmission reconstruction of the object function $F(x, y)$ of figure 3. Laser position at $x_1 = 1$ mm, $f = 15$ Hz; regularization parameter $\sigma = 10^{-9}$.

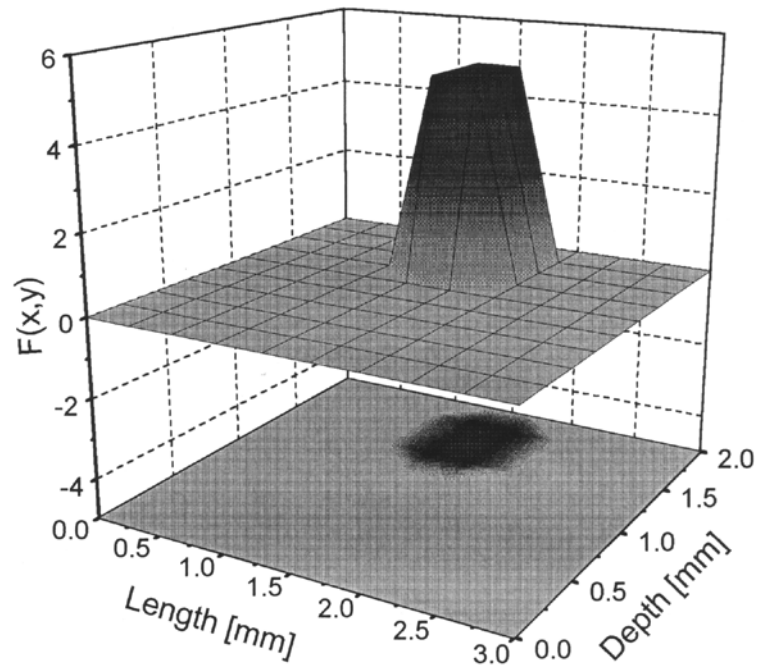


Figure 6. The forward process; three-dimensional relief of a simulated cross section with a hole centred at $(x_c, y_c) = (1.5$ mm, 0.5 mm); radius $a = 0.4$ mm.

The sample region is divided into n intervals, and the rectangular region R is divided into n^2 cells. If the thermal-wave field in transmission $T(x, y = y_f)$ is measured, then from the Born approximation, equation (8), and for $1 \leq j \leq n^2$ the scattering field assumes the following form [8],

$$T_s(j\Delta x, y_f) = \int_{x_i}^{x_f} \int_0^{y_f} G_0[r(j\Delta x, y_f)|r_0(\xi, \eta)]F[r_0(\xi, \eta)]T_i[r_0(\xi, \eta)]d\xi d\eta. \quad (22)$$

Equation (22) can be written in a similar form for the thermal-wave field in back scattering, with $y_f = 0$ in the integrand.

Experimentally, the total transmitted or back-scattered field is measured. The measurement provides the amplitude, $|T|$, and phase, ν , of the field, and, thus, the total field can be expressed in the following complex form,

$$T(\mathbf{r}) = |T(\mathbf{r})| \exp[i\nu(\mathbf{r})]. \quad (23)$$

The total thermal-wave field, $T(\mathbf{r})$, can be expressed as the sum of the incident (homogeneous) field, $T_i(\mathbf{r})$, and of the scattering field, $T_s(\mathbf{r})$, as follows:

$$T(\mathbf{r}) = T_i(\mathbf{r}) + T_s(\mathbf{r}). \quad (24)$$

Using equation (24) with the theoretically calculated incident field, equations (20a) and (20b), the scattered field at the transmitted or back-scattered surface is computed. With the computed scattered field, the theoretical expression of Green's function and the homogeneous temperature distribution, T_i , the object function, $F(\mathbf{r}_0)$, is computed via the inversion of the complex linear system (22). The solution of the complex linear system (22) is a complex function whose real part is the required object function, F , and whose imaginary part is theoretically zero [9]. Numerically, it is not exactly zero, and its value may serve as a criterion/measure for successful reconstruction [9]. The use of the first Born approximation only, while neglecting higher orders, simplifies large-scale computation.

To solve the ill-posed problem in equation (8), Tikhonov's regularization method is used. Let $\mathbf{Ax} = \mathbf{b}$ be an algebraic problem, equivalent to system (8), with \mathbf{A} being ill-conditioned. The regularized solution, \mathbf{x}_σ , as proposed by Tikhonov [20] is

$$\mathbf{x}_\sigma = \min\{\|\mathbf{Ax} - \mathbf{b}\|_2 + \sigma \|\mathbf{L}(\mathbf{x} - \mathbf{x}_0)\|_2\} \quad (25)$$

where \mathbf{x}_0 is an initial estimate of the solution, and matrix \mathbf{L} is either the identity matrix \mathbf{I} or a discrete approximation to a derivative operator. The regularization parameter, σ , controls the weight given to minimization of the side constraint, $\|\mathbf{L}(\mathbf{x} - \mathbf{x}_0)\|_2$, relative to minimization of the residual norm, $\|\mathbf{Ax} - \mathbf{b}\|_2$. For this work, no particular knowledge about the desired solution is available, so $\mathbf{x}_0 = 0$ is used; also matrix \mathbf{L} is set as the identity matrix, \mathbf{I} . It is found that the minimum of equation (25) can be obtained as the solution of the linear system [9]

$$(\sigma\mathbf{I} + \mathbf{A}^*\mathbf{A})\mathbf{x} = \mathbf{A}^*\mathbf{b} \quad (26)$$

where starred quantities denote adjoint matrices.

The fundamental idea in Tikhonov regularization is to introduce a trade-off between the size of the residual norm $\|\mathbf{Ax} - \mathbf{b}\|_2$ and the side constraint $\|\mathbf{x}\|_2$. By choosing a suitable regularization parameter, σ , a satisfactory solution is one for which the two constraints must be balanced [21].

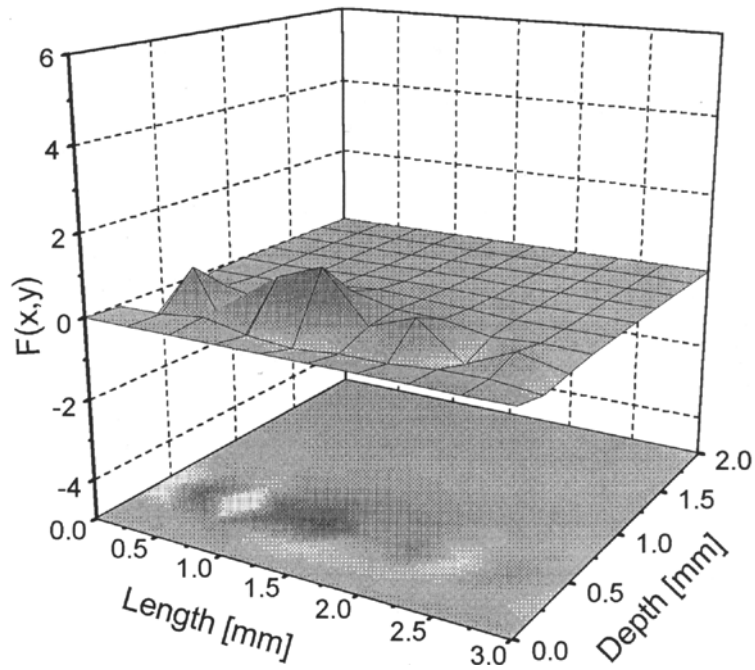


Figure 7. The inverse process-TSDT back-scattering reconstruction of the object function $F(x, y)$ of figure 6. Laser position at $x_1 = 1$ mm, $f = 15$ Hz; regularization parameter $\sigma = 10^{-4}$.

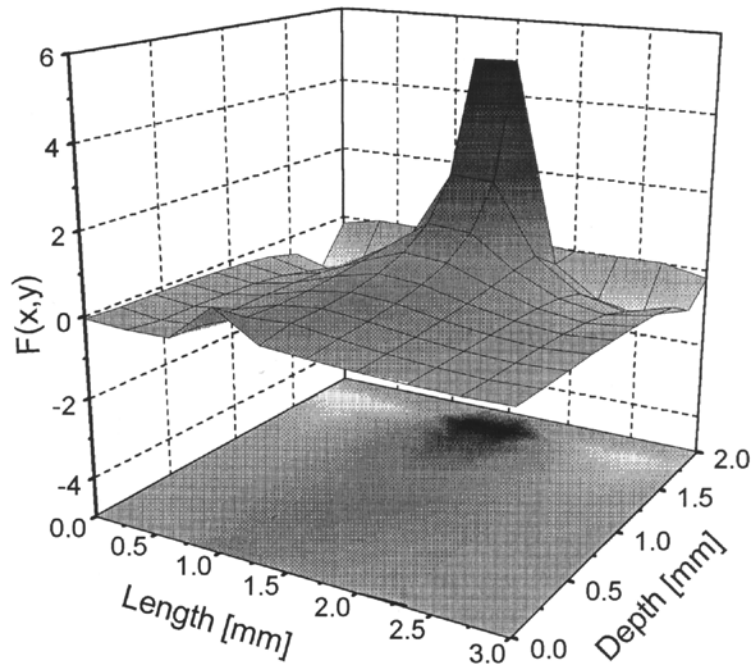


Figure 8. The inverse process-TSDT transmission reconstruction of the object function $F(x, y)$ of figure 6. Laser position at $x_1 = 1$ mm, $f = 15$ Hz; regularization parameter $\sigma = 10^{-9}$.

4. Simulated tomographic inversions

Computer simulations that verify the inversion technique for imaging cross sectional defects are presented. The simulations are produced by solving the exact forward process developed in section 2, with an assumed object function, and, then, inverting the result via the Born approximation of the inverse process method developed in section 3. The object function resulting from the inversion process is compared to the original assumed object function to test the accuracy of the inversion technique. Various classes of defects are investigated in both back-scattering and transmission modes.

4.1. Simulation method

The scattering field, T_s , is solved using a known object function $F(x, y)$. The homogeneous field, T_i , represented by equations (20a) or (20b), is then added to the scattering field by equation (24). The result is the total temperature field that would be obtained under ideal experimental conditions. The amplitude and phase of this field are then calculated and used as input for the inverse process discussed in section 3.

In the simulation of an aluminium sample with a circular hole, the object function is defined as follows,

$$F(x, y) = \begin{cases} 4 & (x - x_c)^2 + (y - y_c)^2 \leq a^2 \\ 0 & \text{otherwise} \end{cases} \quad (27)$$

where x_c, y_c is the centre of the circle and a its radius. The value 4 is chosen because it approximates the ratio of the thermal diffusivities of aluminium and of air, according to equation (6). The input parameters needed for the calculation of the homogeneous field are thermal diffusivity, α , and thermal conductivity, k , of the aluminum sample; the modulation frequency, f ; and the beam size, w , of the laser beam. For the simulations the input values were $\alpha_{Al} = 9.0 \times 10^{-5} \text{ m}^2 \text{ s}^{-1}$, $k_{Al} = 2.37 \times 10^2 \text{ W m}^{-1} \text{ K}^{-1}$, $\alpha_{air} = 2.2 \times 10^{-5} \text{ m}^2 \text{ s}^{-1}$ and $w = 50 \text{ }\mu\text{m}$. The depth of the defect is measured from the front surface of the sample. In the inverse process reconstruction of the object function, $F(x, y)$, the optimal solution to the linear system (26) is given by the Tikhonov regularization parameter that produces an object function with an imaginary part of approximately zero. This criterion has also been used successfully for quantitative thermal-wave microscopy reconstructions [22]. In every reconstruction that was performed, the imaginary part was less than 7% of the object function's magnitude. A 10×10 low-density grid was used and thus the linear system (26) was made up of 100 equations. For some reconstructions a finer grid, of 16×16 was used.

4.2. Computer simulation results and discussion

The computer simulations are separated into three sets in order to address some of the fundamental aspects of TSDT, complementary to earlier conclusions [9]. The first set of defects addresses the effects of the depth of a hole in a rectangular cross section, in both back-scattering and transmission modes (figures 3–8). In the second set, averaging of reconstructions is shown as a method of obtaining an optimal reconstruction. The technique is illustrated in back-scattering mode (figures 9–12). The third set deals with the ability to reconstruct more complex functions such as multiple defects. This set also addresses the resolution of two defects at the same depth as the distance between them decreases, indicated with back-scattering reconstructions (figures 13–17). A finer grid was chosen for these reconstructions to more precisely examine the spatial resolution behaviour. The

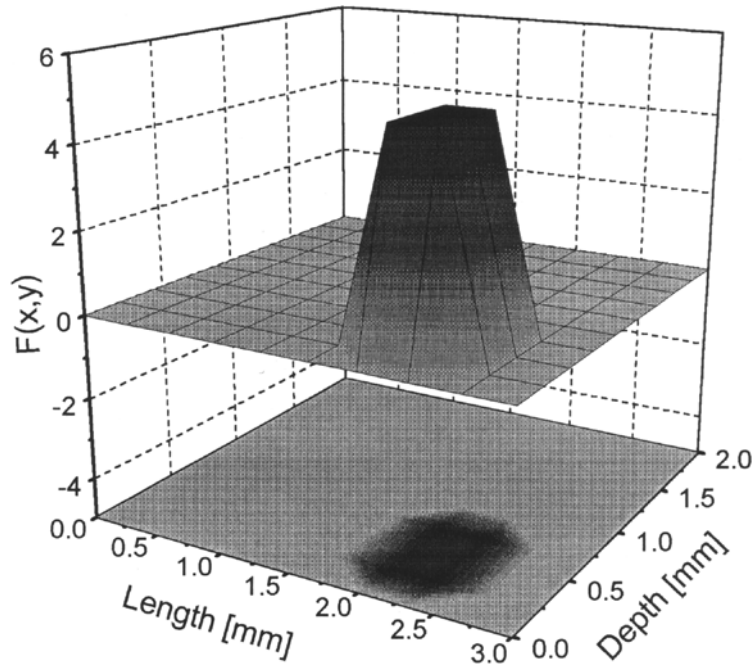


Figure 9. The forward process; three-dimensional relief of a simulated cross section with a hole centred at $(x_c, y_c) = (2.15 \text{ mm}, 0.5 \text{ mm})$; radius $a = 0.4 \text{ mm}$.

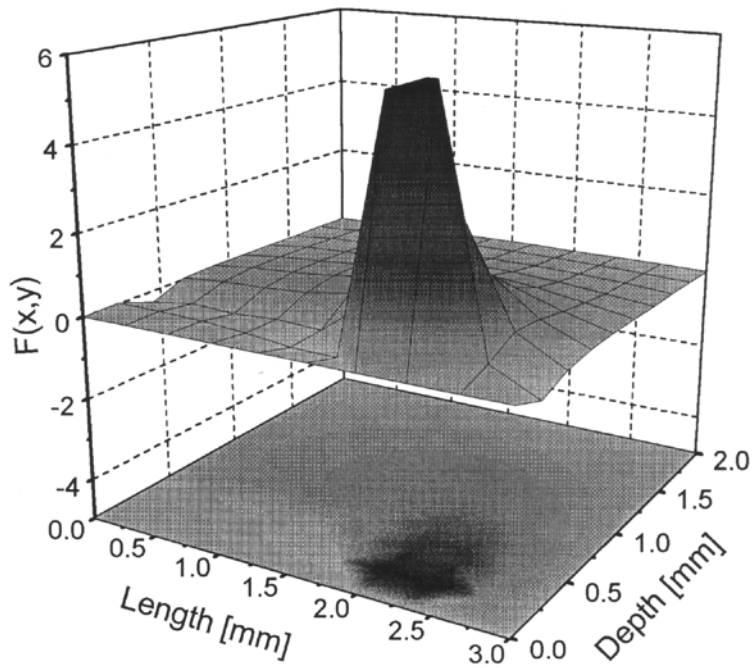


Figure 10. The inverse process—TSDT back-scattering reconstruction of the object function $F(x, y)$ of figure 9. Laser position at $x_1 = 0 \text{ mm}$, $f = 15 \text{ Hz}$; regularization parameter $\sigma = 10^{-6}$.

quality of a reconstruction is rated by the accuracy of three main attributes: defect size, location and magnitude (or contrast). The exact contrast value is 4.

Figure 3 shows the simulated object function, $F(x, y)$, with a filled isometric signal contour of the reconstruction function at the bottom, of a circular hole with radius $a = 0.4$ mm, centred at $(x = 1.5$ mm, $y = 0.5$ mm), in a rectangular cross section of length 3 mm and thickness 2 mm. The defect region does not resemble a circle because of the rough grid size of the rectangular region. A finer grid would improve the image to more closely approximate a circle at the expense of computation time. Figure 4 is the back-scattering reconstruction of figure 3 with the laser position at $x = 1$ mm, a total of 100 detector scan positions, and with a modulating frequency of 15 Hz. When a laser position is given for a specific reconstruction, the position, with respect to the origin, is at the front surface of the rectangular region. The location and contrast of this image are very accurate. The size of the defect, as seen from the front surface, is precise, but the back of the defect is slightly distorted. This occurs because: (a) the information from only one laser source position is used in the reconstruction and (b) the detection occurred at the front surface, in back-scattering mode, where only limited information about the back surface of the defect can be obtained. The quality of the reconstruction is, nevertheless, satisfactory. The regularization parameter used was 10^{-6} , which is relatively high. *The regularization parameter is directly proportional to the ill conditioning of the problem.* An ill-defined problem gives a reasonable solution after being regularized. Figure 5 is the transmission reconstruction of figure 3, with a modulation frequency of 15 Hz, the laser position at $x = 1$ mm, and a total of 100 detector scan positions. The location of the defect is precise but the defect size is decreased and the contrast of the image is poor. An important observation about this reconstruction is that the front surface of the defect is not seen. This is due to the fact that the detection occurred at the back surface and within limited lateral extent, which conceals the front edge of the material. Therefore, only limited information is available to reconstruct the front of the defect. The regularization parameter used was 10^{-9} , so this problem is less ill conditioned than the back-scattering one. Figure 6 is the simulated object function, $F(x, y)$, of a circular hole with radius $a = 0.4$ mm and centred at $(x = 1.5$ mm, $y = 1.5$ mm) in a rectangular cross section of length 3 mm and thickness 2 mm. The defect is now located at the back surface of the material. The back-scattering reconstruction of figure 6 is shown in figure 7. The modulation frequency is 15 Hz, the laser position is at $x = 1$ mm with 100 detector scan positions, and the regularization parameter is 10^{-4} . The quality of this tomogram is very poor. The position of the defect is shifted towards the front surface; also the contrast is diminished, along with the size of the defect. This shifting is a limitation of the back-scattering mode, and is related to the defect depth versus thermal diffusion length relationship: in back scattering, the thermal wave has to travel twice the defect depth for the scatterer to be seen at the front surface. When the defect is deeper, less accurate information about the defect is received at the front surface owing to the large dispersion and diffraction suffered by the thermal waves. Figure 8 is the transmission reconstruction of figure 6, at a modulation frequency of 15 Hz, a laser position at $x = 1$ mm, and the same number of detector scan positions. This is a good reconstruction with a small regularization parameter of 10^{-9} . The location and contrast of the defect is very accurate; the front shape of the defect is diminished and distorted to only a small degree. In transmission, the thermal wave has to travel only the defect depth for the scatterer to be seen at the back surface. Therefore, the imaging fidelity is considerably higher than in the back-scattering mode. Figures 3–8 show that (a) the back-scattering mode gives high-quality tomograms of shallow defects, whereas in the transmission mode, *deep* defects are reconstructed well, (b) back scattering degrades more readily than transmission

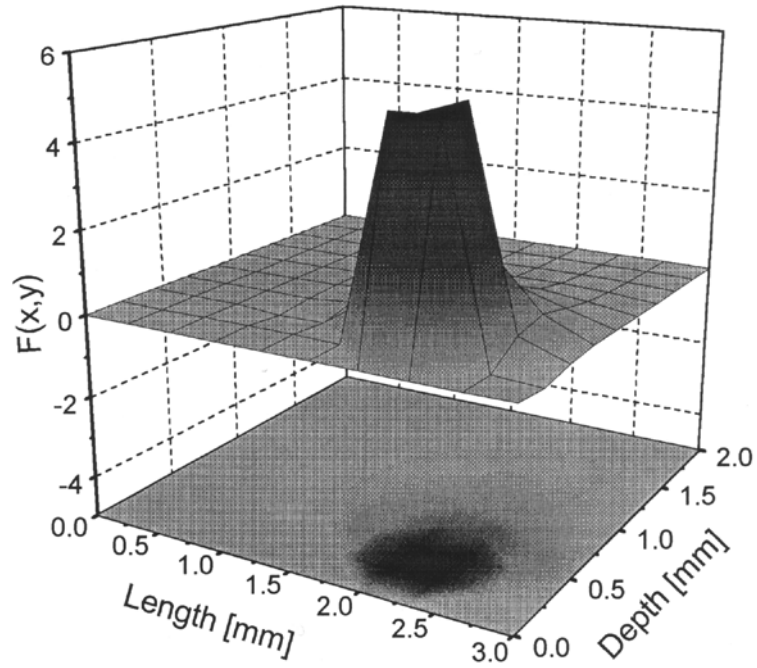


Figure 11. The inverse process–TSDT back-scattering reconstruction of the object function $F(x, y)$ of figure 9. Laser position at $x_1 = 2.3$ mm, $f = 15$ Hz; regularization parameter $\sigma = 10^{-6}$.

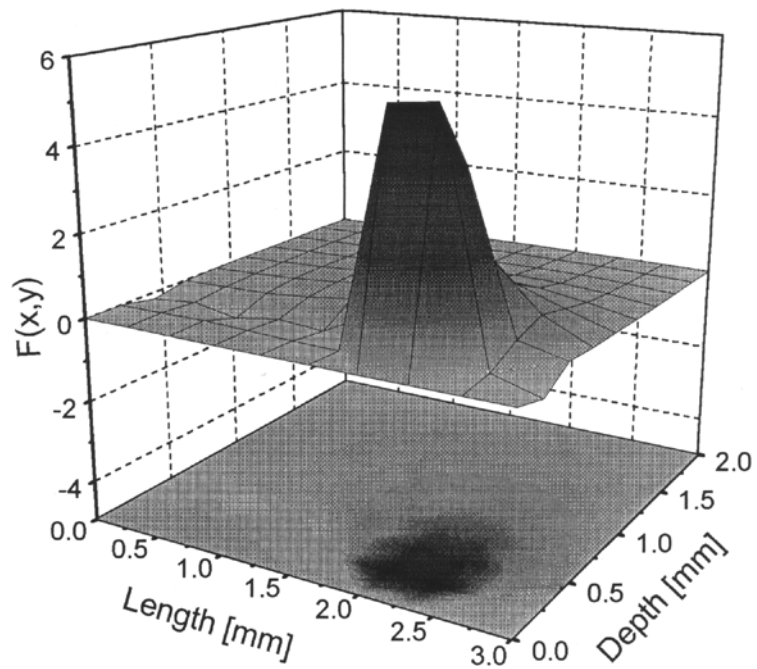


Figure 12. The inverse process–average back-scattering reconstruction of five laser positions.

with increasing defect depth, (c) reconstructions in back scattering are more ill-defined than in transmission, (d) as long as the regularization parameter is within computer accuracy the quality of a reconstruction does not depend on it, but rather depends on the physical characteristics of defect and thermal waves.

The intent of figures 9–12 is twofold. First, the impact of moving the laser position on a reconstruction is illustrated. Second, an optimal reconstruction is achieved by averaging all of the reconstructions at different laser positions. Figure 9 is the simulated object function, $F(x, y)$, in a rectangular cross section of length 3 mm and thickness 2 mm, of a circular hole with radius $a = 0.4$ mm, centred at $x = 2.15$ mm and $y = 0.5$ mm. Figure 10 is the back-scattering reconstruction of the object function, $F(x, y)$, of figure 9 at a modulation frequency of 15 Hz and a regularization parameter of 10^{-6} . The laser position is at the edge of the scan, $x = 0$ mm. 100 detector positions were used in this reconstruction. The location, shape and contrast of the image are satisfactory. The size of the defect is accurate in the front surface, along the side of the defect, where the thermal wave first encounters it (left-hand side). The back of the defect is slightly degraded. Further reconstructions with a single laser-source position gradually approaching the position of the defect were carried out using the same number of detector positions, and showed measurable image improvement. In figure 11, the laser is positioned at $x = 2.3$ mm, placing it above the defect. This laser position gave the most accurate shape, contrast and size of any of the images reconstructed in this set. As the laser moves further away from the defect to $x = 3$ mm, the image contrast is diminished and the size and shape of the defect are distorted. *It can be concluded that the quality of the reconstruction is inversely related to the laser's distance from the defect.* It is interesting to observe that the regularization parameter for all reconstructions at different laser source positions is the same. This implies that the position of the laser beam is not related to the ill-conditioning of the inverse problem. Information of a different kind is obtained at each laser position which is related to the angle from which the thermal wave views the defect. The minimum requirement for reconstructing an image is only one laser position with multiple detection points. Since data at multiple laser positions can be obtained as well, the reconstruction of individual laser positions with multiple detection points is performed, added to a resultant matrix, and divided by the number of laser positions. This process produces an arithmetic average of individual reconstructions and thus an optimal reconstruction. Figure 12 is the average reconstruction of five such reconstructions, including figures 10 and 11. This image has a diminished artefact content and enhanced contrast compared with any of its individual constituents.

For an accurate study of spatial resolution, a fine-density grid of 16×16 was used to solve the linear system of equations (26). Figure 13 shows the simulated object function, $F(x, y)$, of two circular holes with radius $a = 0.15$ mm, centred at $(x = 1.2$ mm, $y = 0.3$ mm) and $(x = 1.8$ mm, $y = 0.3$ mm), in a rectangular cross section of length 3 mm and thickness 1.5 mm. The back-scattering reconstruction of figure 13 at a modulation frequency of 15 Hz is shown in figure 14. At that frequency the thermal diffusion length in aluminium is 2.5 mm and the thermal wavelength is 15.7 mm, greater than the size of these defects. The laser position is at the centre of the scan ($x = 1.5$ mm), in a symmetrical distance from the defects. A total of 256 detector scan positions were used for all fine-grid reconstructions. The distance between the two defects, in terms of grid size ($\Delta x = 0.2$ mm), is 0.2 mm. The actual centre-to-centre distance is 0.6 mm. Both defects are clearly resolved, and the quality of the reconstruction in location, size and contrast, is precise. It is clear that the thermal wavelength is not the limiting factor of resolution [23]. This is due to the fact that the photothermal microscope works in the near-field limit. Figure 15 is the simulated object function, $F(x, y)$, of two circular holes with radius $a = 0.15$ mm,

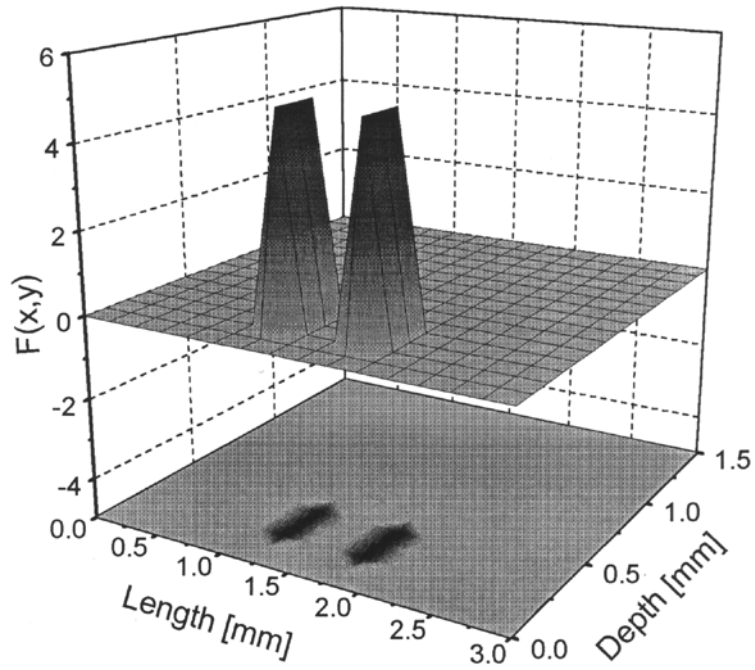


Figure 13. The forward process; three-dimensional relief of a simulated cross section with two holes centred at $(x_c = 1.2$ and 1.8 mm, $y_c = 0.3$ mm); radius $a = 0.15$ mm.

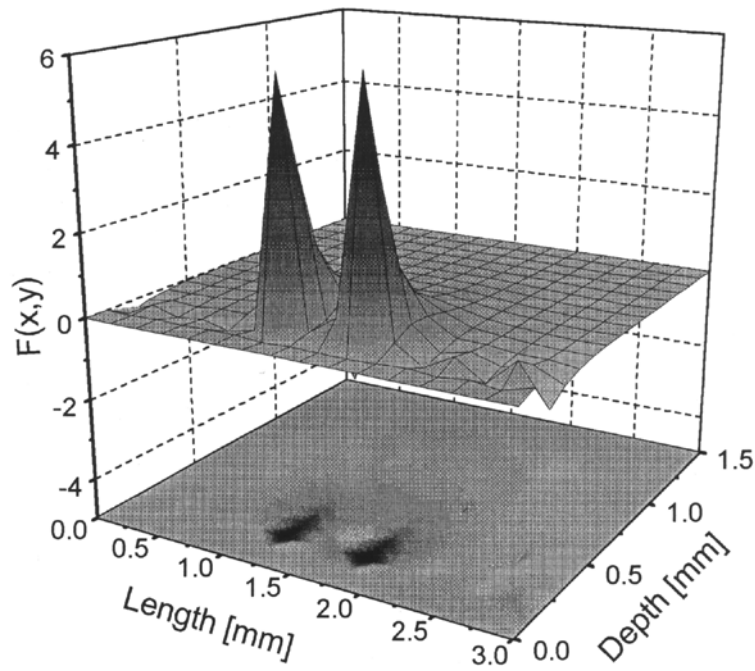


Figure 14. The inverse process—TSDT back-scattering reconstruction of the object function $F(x, y)$ of figure 13. Laser position at $x_1 = 1.5$ mm, $f = 15$ Hz; regularization parameter $\sigma = 10^{-6}$.

centred at $(x = 1.4 \text{ mm}, y = 0.3 \text{ mm})$ and $(x = 1.8 \text{ mm}, y = 0.3 \text{ mm})$, in a rectangular cross section of length 3 mm and thickness 1.5 mm. The defects are not separated by a grid step but are still distinguished from each other. In figure 16, the back-scattering reconstruction, with a modulation frequency of 15 Hz and laser position at $x = 1.6 \text{ mm}$ is shown. At the front boundary the defects are resolved, but as the depth increases the resolution deteriorates. The back surface of the defect is seen as one large defect. Figure 17, is the back-scattering reconstruction with a modulation frequency of 50 Hz and laser position at $x = 1.6 \text{ mm}$. As the frequency increases the resolution at the front defect boundary improves. As expected, information about the back of the defect is lost. Therefore, increasing depth and decreasing frequency leads to a lower spatial resolution and poor delineation of subsurface thermal boundaries. This type of behaviour has been observed and extensively studied in conventional thermal-wave imaging [23] and in ray-optic tomographic thermal-wave imaging [6].

The Born approximation seems to be adequate for the materials and defect geometries utilized in this investigation. Assuming tubular (cylindrical) defects, such as drilled holes in aluminium, Kak and Slaney [11] have given a mathematical condition of the validity of the first Born approximation for general propagating fields obeying the conventional Helmholtz wave equation. This condition can be expressed as

$$an_\delta < \frac{\lambda}{4} \quad (28)$$

where a is the radius of the cylindrical defect, n_δ is the change in the refractive index between the surrounding medium and the defect, and λ is the probe-field wavelength. For the worst-case situation of thermal-wave tomography examined in this work, $a = 0.4 \text{ mm}$, $\lambda_{\text{th}} = 4.76 \text{ mm}$ at 50 Hz and $n_\delta = 2.02$, equation (6). Therefore, $an_\delta = 0.81 \text{ mm} < 1.19 \text{ mm} = \lambda_{\text{th}}/4$, i.e. the criterion (30) holds for thermal-wave tomography, as well.

5. Conclusions

An improved TSDT reconstruction method was based on solving the Helmholtz pseudowave equation with a complex wavenumber [10], for the thermal-wave field generated in a material by some convenient means, such as an intensity-modulated laser beam incident on the (opaque) surface. The three-dimensional incident field, assuming Neumann boundary conditions, was calculated based on the known expression of Green's function [12], and a novel exact expression of the pseudopropagating three-dimensional thermal-wave field was derived. Ultimately, the scattered field was expressed in the first Born approximation by a Fredholm integral equation of the first kind. Owing to the diffusive nature of the thermal-wave field and the ill-conditioning of the inverse problem, conventional Fourier transform methods used in electromagnetic and acoustic tomography did not apply [11]. Thus, the integral equation was solved using the Tikhonov regularization method. Numerical simulations were then performed to test the method.

From the above simulations, it was seen that the Born approximation yields a large number of satisfactory results. Shallow defects were imaged better in back scattering and deep defects were imaged better in transmission. The back scattering mode is more ill-conditioned than the transmission mode. Increasing the modulation frequency causes small changes in back-scattering reconstruction when the defect is within one thermal diffusion length from the front surface, while it leads to a marked image deterioration as the modulation frequency is increased beyond this limit. For shallow defects, transmission reconstruction is more sensitive to changes in modulation frequency than back-scattering

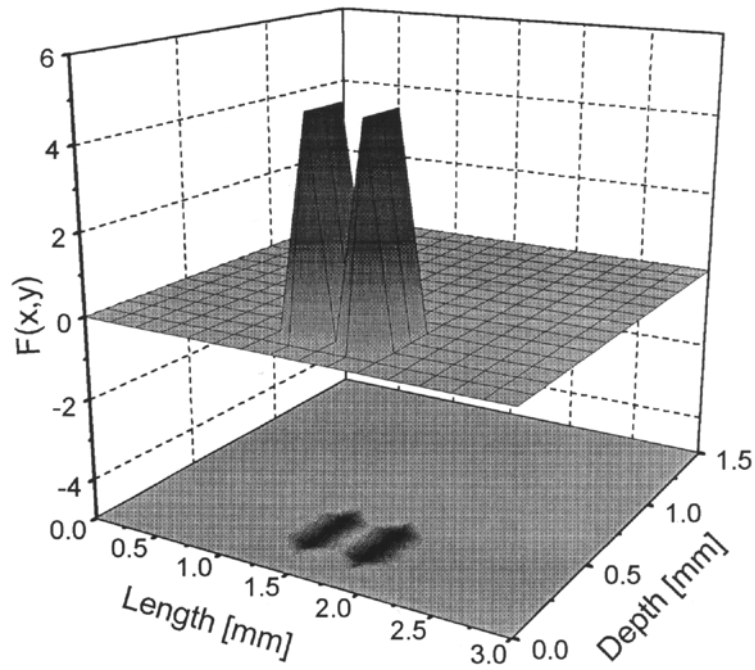


Figure 15. The forward process; three-dimensional relief of a simulated cross section with two holes centred at $(x_c = 1.4$ and 1.8 mm, $y_c = 0.3$ mm); radius $a = 0.15$ mm.

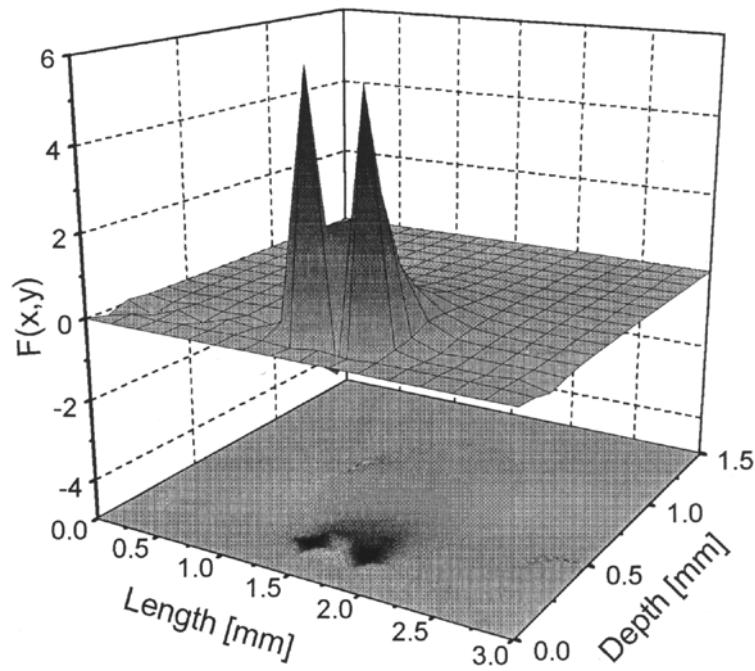


Figure 16. The inverse process—TSDT back-scattering reconstruction of the object function $F(x, y)$ of figure 15. Laser position at $x_1 = 1.6$ mm, $f = 15$ Hz; regularization parameter $\sigma = 10^{-6}$.

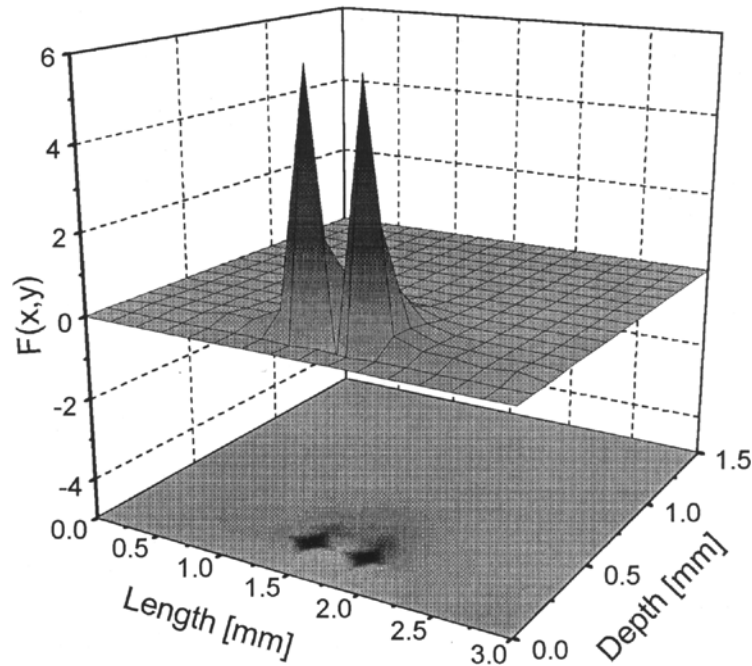


Figure 17. The inverse process-TSDT back-scattering reconstruction of the object function $F(x, y)$ of figure 15. Laser position at $x_1 = 1.6$ mm, $f = 50$ Hz; regularization parameter $\sigma = 10^{-6}$.

reconstruction. The shape of a defect is reconstructed accurately on the side of the defect that the thermal wave first encounters it. The minimum requirement for reconstructing the cross sectional thermal diffusivity image is a single laser position and several detector scan positions, or vice versa. A defect can be reconstructed at different laser positions, and the accuracy of the reconstruction is inversely related to the laser's distance from the defect. Since only limited information is obtained from one laser position reconstruction, an arithmetically averaged reconstruction of different laser positions leads to an optimal image, especially when the actual subsurface position of a defect is unknown and in the presence of artefacts. Finally, spatial resolution is lost with increasing depth and decreasing frequency.

Overall, the physical behaviour of the numerical simulations validates the new theoretical model developed for the three-dimensional incident and scattered fields. Based on considerations adapted from propagating-field tomographies, the Born approximation seems to be a valid approximation for the parameter ranges of this work, albeit no rigorous mathematical proof of its validity was given.

Acknowledgments

The support of the Natural Sciences and Engineering Research Council of Canada (NSERC) and of the Manufacturing Research Corporation of Ontario (MRCO) is gratefully acknowledged.

References

- [1] Busse G and Renk K F 1983 Stereoscopic depth analysis by thermal wave transmission for non-destructive evaluation *Appl. Phys. Lett.* **42** 366
- [2] Busse G 1983 Thermal wave non-destructive depth profiling with stereoscopic photothermal detection *J. Physique* **44** 471
- [3] Fournier D, Lepoutre F and Boccara A C 1983 Tomographic approach for photothermal imaging using the mirage effect *J. Physique* **44** 479
- [4] Mandelis A and Mieszkowski M 1990 Thermal wave sub-surface defect imaging and tomography apparatus *US Patent No 4950897*
- [5] Munidasa M and Mandelis A 1991 Photopyroelectric thermal-wave tomography of aluminum with ray-optic reconstruction *J. Opt. Soc. Am. A* **8** 1851
- [6] Munidasa M, Mandelis A and Ferguson C 1992 Resolution of photothermal tomographic imaging of sub-surface defects in metals with ray-optic reconstruction *Appl. Phys.* **54** 244
- [7] Yagai A, Sakamoto K and Nakanishi T 1994 High signal-to noise ratio and high resolution detection techniques for photopyroelectric thermal wave imaging reconstruction *J. Appl. Phys., Japan* **33** 3255
- [8] Padé O and Mandelis A 1994 Thermal-wave slice tomography using wave-field reconstruction *Inverse Problems* **10** 185
- [9] Padé O and Mandelis A 1993 Computational thermal-wave slice tomography with backpropagation and transmission reconstructions *Rev. Sci. Instrum.* **64** 3548
- [10] Mandelis A 1991 Theory of photothermal wave diffraction tomography via spatial laplace spectral decomposition *J. Phys. A: Math. Gen.* **24** 2485
- [11] Kak A C and Slaney M 1988 *Principles of Computerized Tomographic Imaging* (New York: IEEE)
- [12] Mandelis A 1995 Green's functions in thermal wave physics: Cartesian coordinate representations *J. Appl. Phys.* **78** 647
- [13] Nicolaidis L, Munidasa M and Mandelis A 1997 Thermal-wave infrared radiometric slice diffraction tomography with back scattering and transmission reconstructions: experimental *Inverse Problems* **13** 1413
- [14] Mandelis A 1989 Theory of photothermal-wave diffraction and interference in condensed media *J. Opt. Soc. Am. A* **6** 298
- [15] Morse P M and Feshbach H 1953 *Methods of Theoretical Physics* (New York: McGraw-Hill) ch 7
- [16] Langenberg K J 1986 *Applied Inverse Problems, (Notes on Summer School on Applied Inverse Problems)* Fachgebiet Theoretische Elektrotechnik der Gesamthochschule, Kassel, GHK-TET, Kassel, ch 3
- [17] Abramowitz M and Stegun A 1970 *Handbook of Mathematical Functions* 9th edn (Washington, DC: National Bureau of Standards)
- [18] Morozov V A 1993 *Regularization Methods for Ill-posed Problems* (Boca Raton, FL: Chemical Rubber Company)
- [19] Tarantola A 1987 *Inverse Problem Theory* (New York: Elsevier)
- [20] Hofmann B 1986 *Regularization for Applied and Ill-posed Problems* (Leipzig: Teubner)
- [21] Hansen C 1992 Numerical tools for analysis and solution of fredholm integral equations of the first kind *Inverse Problems* **8** 849
- [22] Seidel U, Haupt K, Walther H G, Burt J A and Munidasa M 1993 An attempt towards quantitative photothermal microscopy *J. Appl. Phys.* **78** 2050
- [23] Munidasa M and Mandelis A 1992 *Principles and Perspectives of Photothermal and Photoacoustic Phenomena* ed A Mandelis (New York: Elsevier) pp 300–58